

Strong electron-phonon coupling in the intermetallic superconductor $\text{Mo}_8\text{Ga}_{41}$ Valeriy Yu. Verchenko,^{1,2,*} Alexander A. Tsirlin,^{2,3,†} Alexander O. Zubtsovskiy,¹ and Andrei V. Shevelkov¹¹*Department of Chemistry, Lomonosov Moscow State University, 119991 Moscow, Russia*²*National Institute of Chemical Physics and Biophysics, 12618 Tallinn, Estonia*³*Experimental Physics VI, Center for Electronic Correlations and Magnetism, Institute of Physics, University of Augsburg, 86135 Augsburg, Germany*

(Received 4 November 2015; revised manuscript received 18 December 2015; published 1 February 2016)

Crystals of superconducting $\text{Mo}_8\text{Ga}_{41}$ ($T_c = 9.8$ K) and $\text{Mo}_{8-x}\text{V}_x\text{Ga}_{41}$ limited solid solution [$x_{\text{max}} = 1.9(2)$] have been grown from the high-temperature Ga flux and confirmed to have the V_8Ga_{41} type of crystal structure at room temperature. Thermodynamic and transport measurements as well as electronic structure calculations were performed to investigate both normal- and superconducting-state properties of $\text{Mo}_8\text{Ga}_{41}$. The discontinuity in the heat capacity at T_c , $\Delta C_p/\gamma_N T_c = 2.83$ in zero magnetic field, indicates a much stronger electron-phonon coupling than in the standard BCS limit. From the heat-capacity data, we estimated the electron-phonon coupling constant $\lambda_{ep} = 0.9$. The upper critical field is $\mu_0 H_{c2}(0) = 8.3$ T, while the lower one is only $\mu_0 H_{c1}(0) = 131$ Oe. The upper critical field of $\text{Mo}_8\text{Ga}_{41}$ exhibits a clear enhancement with respect to the Werthamer-Helfand-Hohenberg prediction, consistent with the strong electron-phonon coupling. The $\text{Mo}_{8-x}\text{V}_x\text{Ga}_{41}$ limited solid solution also exhibits superconducting properties, and the critical temperature T_c is reduced only slightly with increasing x .

DOI: 10.1103/PhysRevB.93.064501

I. INTRODUCTION

In previous decades, the investigation of superconductors was aimed at either finding materials with higher critical temperature T_c , or discovering nontypical superconducting behavior that significantly deviates from the conventional BCS model. Mo-based compounds attract interest in the light of both these goals. Several Mo-based carbides were reported to be superconductors with relatively high transition temperatures: γ - MoC with $T_c = 9.3$ K [1], η - MoC_{1-x} (8.9 K [1]), α - Mo_2C (6.1 K [2]), β - Mo_2C (5.2 K [2]), and $\text{Mo}_3\text{Al}_2\text{C}$ (9.05 K [3]). The latter compound is a noncentrosymmetric superconductor. Initially, it was ascribed to a strong-coupling regime with noticeable deviations from the BCS model [3,4]. However, magnetic penetration depth measurements evidenced nodeless energy gap and established the conventional behavior of $\text{Mo}_3\text{Al}_2\text{C}$ [5]. In a recent study [6], the muon spin relaxation rate measurements did not reveal any indications of time-reversal symmetry breaking in $\text{Mo}_3\text{Al}_2\text{C}$ and confirmed that this compound features a single s -wave superconducting gap.

Among Mo-based compounds, Mo_3Sb_7 also attracts interest because of its complex behavior at low temperatures. Two transitions that are observed in this compound at 2.3 and 50 K can be attributed to the formation of a superconducting state and spin gap, respectively [7,8]. Therefore, Mo_3Sb_7 can be classified as a system where superconductivity and spin fluctuations coexist, thus resembling the behavior of superconductors with strong electronic correlations [8]. The investigation of Mo_3Sb_7 by means of muon spin relaxation measurements revealed two possibilities to explain the superconducting properties: a single s -wave superconducting gap scenario [9,10] and a double-gap s -wave model [11,12]. The ambiguity between these two scenarios is so far unresolved, although the gap anisotropy and the presence of nodes are

clearly excluded by the recent study of heat transport in Mo_3Sb_7 at low temperatures [13].

Searching for other Mo-based superconductors, which may demonstrate nontypical behavior, we focused on $\text{Mo}_8\text{Ga}_{41}$ intermetallic compound. Earlier, Bezingue and Yvon [14] reported the superconductivity of $\text{Mo}_8\text{Ga}_{41}$ at $T_c = 9.7$ K with the upper critical field $\mu_0 H_{c2} = 8.6$ T at zero temperature. $\text{Mo}_8\text{Ga}_{41}$ crystallizes in the centrosymmetric three-dimensional V_8Ga_{41} type of crystal structure [14,15]. The relatively high values of the transition temperature T_c and upper critical field $\mu_0 H_{c2}$ call for a detailed study of both normal- and superconducting-state properties that have not been addressed in the previous literature.

Here, we report crystal growth of the intermetallic $\text{Mo}_8\text{Ga}_{41}$ as well as the $\text{Mo}_{8-x}\text{V}_x\text{Ga}_{41}$ limited solid solution on its base. Electrical resistivity, isothermal magnetization, magnetic susceptibility and heat-capacity measurements, and electronic structure calculations were performed to investigate both normal- and superconducting-state properties. By revisiting $\text{Mo}_8\text{Ga}_{41}$, we aim to provide insight into microscopic features and electronic structure of this compound.

II. EXPERIMENTAL DETAILS

Crystals of $\text{Mo}_{8-x}\text{V}_x\text{Ga}_{41}$ ($x = 0, 1$, and 2) were grown with a high-temperature solution growth method using Ga both as a reagent and flux medium. Mo powder (99.99%, Sigma Aldrich), V pieces (99.9%, Sigma Aldrich), and Ga pieces (99.999%, Sigma Aldrich) were used as starting materials. According to the standard ampoule technique, they were weighed in the $\text{Mo}:\text{V}:\text{Ga} = (8-x):x:400$ molar ratio and placed inside quartz ampoules, which were then sealed under vacuum at pressure less than 10^{-2} Torr. Ampoules were annealed in a programmable furnace at 830°C for 55 h and slowly cooled to 170°C at the rate of $4^\circ\text{C}/\text{h}$. After synthesis, the excess of liquid Ga was separated using an Eppendorf 5804R centrifuge, yielding well-shaped silvery-gray crystals (inset of Fig. 1). The obtained crystals were purged from the

*verchenko@inorg.chem.msu.ru

†altsirlin@gmail.com

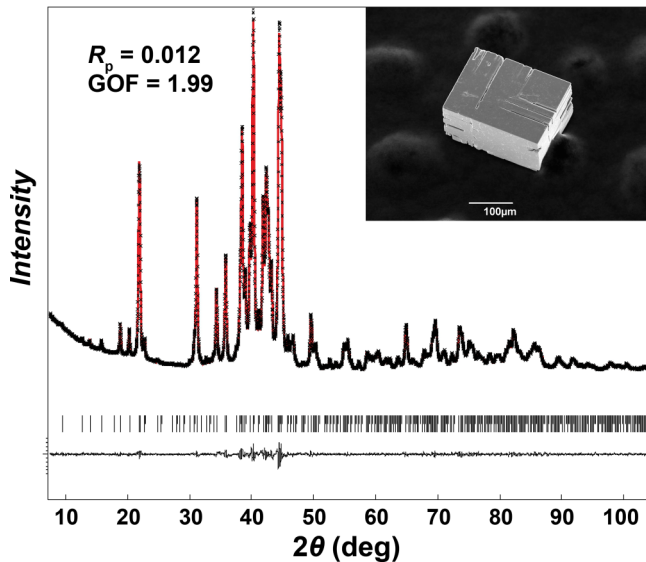


FIG. 1. Experimental (black points) and calculated (red line) XRD patterns of $\text{Mo}_8\text{Ga}_{41}$. Peak positions are given by black ticks; the difference plot is shown as a black line in the bottom part. The inset shows scanning electron microscope image of a typical $\text{Mo}_8\text{Ga}_{41}$ crystal, grown from Ga flux.

remainder of Ga metal with diluted 0.5 M HCl during 24 h and washed with distilled water and acetone.

Powder x-ray-diffraction data were collected at room temperature using a PANalytical X'Pert³ powder diffractometer with Cu $K\alpha$ radiation in the 2θ range between 7.5° and 104° . The data were analyzed by the Rietveld method in JANA2006 software [16].

Crystals were analyzed using a scanning electron microscope JSM JEOL 6490-LV operated at 30 kV and equipped with an EDX detection system INCA x-Sight. Before operation, the EDX detection system was optimized using elemental Co as a standard. To perform quantitative elemental analysis, the system was calibrated with the use of elemental Mo and V, and GaP polished samples. All standards are provided by MAC Analytical Standards.

Several rectangular-shaped single crystals of $\text{Mo}_{8-x}\text{V}_x\text{Ga}_{41}$ were picked from the specimens with $x = 0, 1$, and 2 for the subsequent crystal structure determination and refinement. Data sets were collected from the qualitatively best single crystals on a STOE STADIVARI Pilatus diffractometer equipped with a graphite monochromator and a Mo x-ray source ($\lambda_{\text{Mo}} = 0.71073 \text{ \AA}$). Details of the single-crystal x-ray diffraction (XRD) experiments are presented in Table S1 of the Supplemental Material [17]. After the numerical absorption correction, which was performed by a multiscan routine, the crystal structure was solved by direct methods [18] and refined against F^2 with JANA2006 software [16]. The obtained atomic coordinates and selected interatomic distances are listed in Tables S2 and S3 of the Supplemental Material [17]. The atomic coordinates were standardized by the STRUCTURE TIDY program [19].

Unfortunately, individual single crystals were not large enough for thermodynamic measurements. Therefore, several $\text{Mo}_{8-x}\text{V}_x\text{Ga}_{41}$ ($x = 0, 1$, and 2) crystals were glued together

and measured as polycrystalline samples. The temperature dependencies of the magnetic susceptibility and isothermal magnetization were measured using a superconducting quantum interference device magnetometer (MPMS, Quantum Design) in magnetic fields between 0 and 7 T at temperatures between 1.8 and 300 K. Additionally, isothermal magnetization curves were obtained using the VSM setup of a physical property measurement system (PPMS, Quantum Design) in magnetic fields up to 14 T. The heat-capacity measurements were performed with a relaxation-type calorimeter (HC option, PPMS, Quantum Design) in magnetic fields between 0 and 11 T at temperatures between 1.8 and 20 K.

To investigate transport properties, crystals were crushed in an agate mortar and pressed into rectangular-shaped pellets at the external pressure of 100 bars at room temperature. Densities of the pellets were estimated from their masses and linear sizes to be 87%, 84%, and 86% from the theoretical densities for $x = 0, 1$, and 2 , respectively. Electrical contacts (Cu wire, $50 \mu\text{m}$) were fixed using silver-containing epoxy resin (Epotek H20E) hardened at 120°C , and the resistance was measured by the standard four-probe method using the ac transport setup of PPMS in magnetic fields between 0 and 11 T at temperatures between 1.8 and 400 K with a field applied perpendicular to the direction of current.

The electronic structure of $\text{Mo}_8\text{Ga}_{41}$ was calculated within the local-density approximation (LDA) [20] of the density functional theory (DFT) as implemented in the full-potential FPLO code (version 14.00-47) [21] with the basis set of local orbitals. The integrations in k space were performed by the improved tetrahedron method [22] on a grid of $16 \times 16 \times 16$ k points for the scalar relativistic calculation. The density of states at the Fermi level in the case of $\text{Mo}_{8-x}\text{V}_x\text{Ga}_{41}$ solid solution was calculated using the rigid-band shift approximation.

III. RESULTS AND DISCUSSION

A. Crystal structure of $\text{Mo}_8\text{Ga}_{41}$

The powder XRD pattern of crushed crystals of $\text{Mo}_8\text{Ga}_{41}$ is shown in Fig. 1. All lines in the pattern could be indexed in the $R\bar{3}$ (no. 148) space group, confirming phase purity of the sample. The respective Rietveld refinement of the data yields the cell parameters $a = 14.0454(2) \text{ \AA}$ and $c = 15.0525(2) \text{ \AA}$, which are in good agreement with the previously reported values [15].

A suitable single crystal with the composition $\text{Mo}_{8.1(2)}\text{Ga}_{40.9(2)}$, confirmed by EDX spectroscopy, was selected from the reaction products to perform structure determination. The collected data could be indexed with the cell parameters $a = 14.0290(9) \text{ \AA}$ and $c = 15.0414(9) \text{ \AA}$ in the $R\bar{3}$ (no. 148) space group, which was chosen on the basis of systematic extinction conditions. Atomic positions were determined by direct methods and refined in full-matrix anisotropic approximation. Details of the data collection and refinement are summarized in Table S1 of the Supplemental Material; the atomic parameters and selected interatomic distances are given in Tables S2 and S3, respectively. Our refinement shows that $\text{Mo}_8\text{Ga}_{41}$ crystallizes in the V_8Ga_{41} type of crystal structure, in agreement with the previously

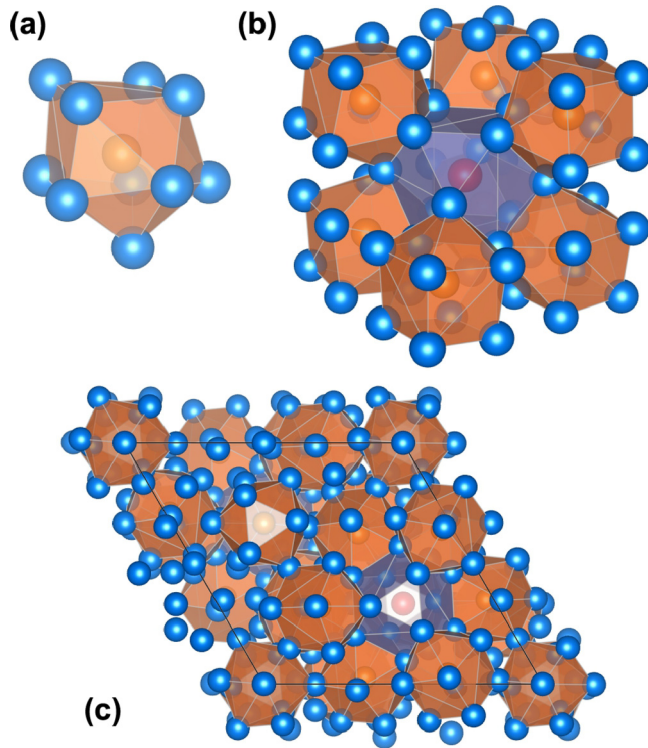


FIG. 2. $\text{Mo}_8\text{Ga}_{41}$ crystal structure: (a) MoGa_{10} polyhedron (orange), (b) the main building block, constructed by MoGa_{10} polyhedra (orange) and GaGa_{12} cuboctahedra (blue), (c) the unit cell content.

reported results [14,15]. The refinement indicates the absence of partially occupied positions in the crystal structure, thus confirming that $\text{Mo}_8\text{Ga}_{41}$ is a stoichiometric compound.

In the $\text{Mo}_8\text{Ga}_{41}$ crystal structure, Mo and Ga atoms occupy two and nine crystallographic positions, respectively. Mo atoms are well separated from each other, and, consequently, only Ga atoms appear in the first coordination sphere of Mo, which is presented by MoGa_{10} polyhedra for both the Mo1 and Mo2 positions. The MoGa_{10} polyhedron [Fig. 2(a)] consists of one half of a $\text{MoGa}_{8/2}$ cube and one half of a $\text{MoGa}_{12/2}$ icosahedron. MoGa_{10} polyhedra are interconnected by corners and form the arrangement, in which one triangular face of each polyhedron is shared with a cuboctahedron centered by the unique Ga atom [Fig. 2(b)]. The Ga atom in the center of a cuboctahedron [crystallographic position $3b$ (0; 0; 0.5)] has no contacts with Mo atoms in the first coordination sphere. Eight MoGa_{10} polyhedra are condensed on the faces of a cuboctahedron, which is occupied by one Ga atom, yielding the $8\text{MoGa}_{10/2} + 1\text{Ga} = \text{Mo}_8\text{Ga}_{41}$ composition of the compound. This arrangement represents a building block of the $\text{Mo}_8\text{Ga}_{41}$ crystal structure, which is clearly three dimensional with Mo atoms being evenly distributed in the matrix of Ga atoms [Fig. 2(c)].

B. Electrical resistivity

The temperature dependence of the $\text{Mo}_8\text{Ga}_{41}$ electrical resistivity, measured in zero magnetic field, is shown in Fig. 3. The $\rho(T)$ exhibits metallic behavior with rather high absolute values of resistivity well above the Mott-Ioffe-Regel limit

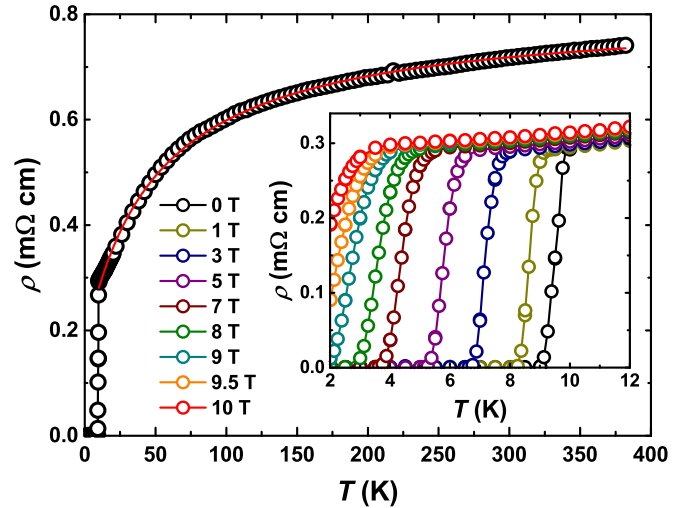


FIG. 3. Electrical resistivity of $\text{Mo}_8\text{Ga}_{41}$ in zero magnetic field. The solid curve represents a fit according to the parallel resistance model. The inset shows resistivity at low temperatures in different applied fields.

($\sim 0.1 \text{ m}\Omega \text{ cm}$). Moreover, at temperatures above 75 K the resistivity grows much slower than at low temperatures. Such behavior was observed in many metallic systems with large resistivity [23], particularly, in strong-coupled transition-metal A15 superconductors [24]. The saturation of resistivity in these compounds occurs when the mean electron free path is comparable to the interatomic distances [23,24]. To account for the saturation of resistivity at high temperatures, the parallel resistance model was used, in which $\frac{1}{\rho(T)} = \frac{1}{\rho_{\text{sat}}} + \frac{1}{\rho_{\text{ideal}}(T)}$. We used a linear behavior for the ideal resistivity: $\rho_{\text{ideal}}(T) = \rho_0 + \alpha T$. A fit employing this model is shown in Fig. 3 by the solid red line and yields $\rho_0 = 0.221(5) \text{ m}\Omega \text{ cm}$ and $\rho_{\text{sat}} = 0.808(2) \text{ m}\Omega \text{ cm}$.

At low temperatures, the resistivity of $\text{Mo}_8\text{Ga}_{41}$ clearly indicates a superconducting transition at $T_c = 9.8 \text{ K}$, where T_c was determined as an onset temperature of the sharp resistivity drop. The obtained value of T_c is in agreement with the data reported by Bezingue and Yvon [14]. The inset of Fig. 3 shows the $\rho(T)$ around the transition in various magnetic fields. As expected, magnetic field shifts the superconducting transition to lower temperatures. These data were used to extract the upper critical field at the transition temperature T_c , which was determined as an onset temperature of the resistive drop. The upper critical field $\mu_0 H_{c2}(T)$ of $\text{Mo}_8\text{Ga}_{41}$ is shown in Fig. 8 and will be discussed further in the text.

C. Magnetic susceptibility

The normal-state magnetic susceptibility of $\text{Mo}_8\text{Ga}_{41}$, measured in the temperature range between 10 and 300 K in the $H = 2 \text{ T}$ magnetic field, is shown in Fig. 4(a). The compound exhibits bulk diamagnetism with the upturn of the magnetic susceptibility at low temperatures $T < 100 \text{ K}$, which is most likely due to paramagnetic impurities. Temperature dependence of the magnetic susceptibility can be satisfactorily fitted with the equation $\chi(T) = \chi_{\text{int}} + C/T$, resulting in the intrinsic susceptibility $\chi_{\text{int}} = -4.96(8) \times 10^{-4} \text{ emu mol}^{-1}$ and

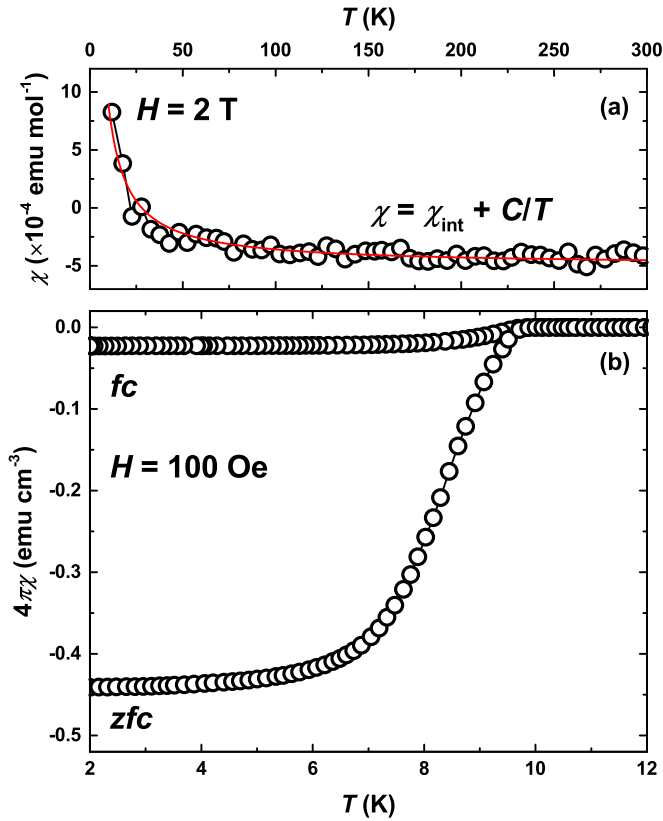


FIG. 4. (a) Normal-state magnetic susceptibility of $\text{Mo}_8\text{Ga}_{41}$ measured at $H = 2$ T; (b) magnetic susceptibility at $H = 100$ Oe, measured in zero-field-cooled and field-cooled conditions.

$C = 0.0139(4)$ emu K mol $^{-1}$. The intrinsic susceptibility χ_{int} includes the following summands: $\chi_{\text{int}} = \chi_{\text{P}} + \chi_{\text{core}} + \chi_{\text{VV}} + \chi_{\text{L}}$, where χ_{P} is the Pauli paramagnetic spin susceptibility of the conduction electrons, χ_{core} is the diamagnetic orbital contribution from the electrons (ionic or atomic), χ_{VV} is the Van Vleck paramagnetic orbital contribution, and χ_{L} is the Landau orbital diamagnetism of the conduction electrons. A realistic estimation of χ_{P} from the above equation is problematic, mostly because of uncertainty in the calculation of the χ_{core} value. For instance, the χ_{core} value for Mo ions gradually decreases from -7×10^{-6} emu mol $^{-1}$ for Mo^{6+} to -31×10^{-6} emu mol $^{-1}$ for Mo^{2+} species [25]. However, chemical bonding in $\text{Mo}_8\text{Ga}_{41}$ is neither ionic nor covalent, therefore, the core contribution is hard to estimate precisely.

The sample contains minor amount of paramagnetic impurities resulting in a Curie-like C/T contribution to χ . The obtained value of C is equal to the presence of 3.7 mol.% of the $S = \frac{1}{2}$ paramagnetic impurity assuming $g = 2$. This impurity contribution can be attributed to the defects induced by the postsynthetic treatment of $\text{Mo}_8\text{Ga}_{41}$ crystals with diluted 0.5M HCl. However, these impurities should not affect other physical properties, such as electrical resistivity and heat capacity of $\text{Mo}_8\text{Ga}_{41}$.

The temperature dependence of the zero-field-cooled (ZFC) and field-cooled (FC) magnetic susceptibilities of $\text{Mo}_8\text{Ga}_{41}$, measured in 100 Oe magnetic field, is shown in Fig. 4(b). The divergence of the ZFC and FC curves indicates a transition to the superconducting state at $T_c = 9.8$ K, in good agreement

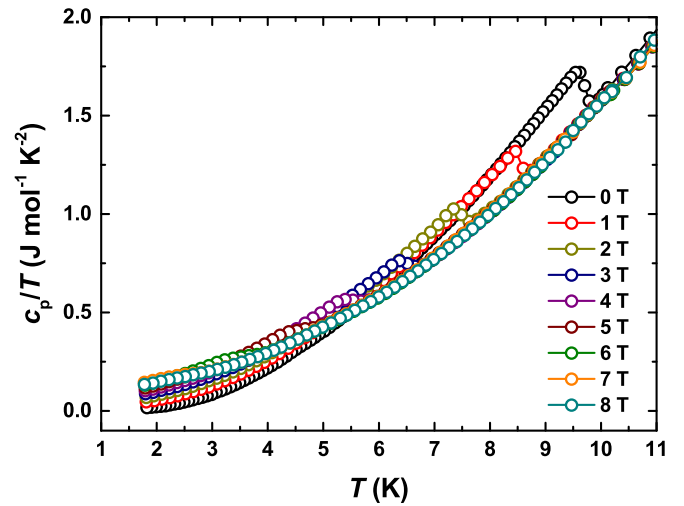


FIG. 5. Specific heat c_p/T vs T plot in various magnetic fields for $\text{Mo}_8\text{Ga}_{41}$.

with the resistivity data. The FC signal (Meissner effect) is weak, which is most probably due to strong flux line pinning in this type-II superconductor. For the ZFC signal, the transition is significantly broadened with temperature, having the width of about 5 K. The reduced volume susceptibility $4\pi\chi$ reaches -0.44 emu cm $^{-3}$ at $T = 2$ K, however, the data were not corrected for the demagnetization effect, since the sample shape is not well defined. Assuming the complete diamagnetic response of the specimen, one obtains the demagnetization factor of 2.3, which is somewhat larger than the value of 1.0 expected for an ellipsoid of revolution.

The isothermal magnetization data were used to estimate both lower $\mu_0 H_{c1}(T)$ and upper $\mu_0 H_{c2}(T)$ critical fields of $\text{Mo}_8\text{Ga}_{41}$ (Fig. 8). $\mu_0 H_{c1}(T)$ was determined as a field, at which the $M(H)$ dependence deviates from a linear behavior with the probability of 95% in the low-field $M(H)$ data. $\mu_0 H_{c2}(T)$ was determined as a kink on the high-field $M(H)$ curve.

D. Heat capacity

The specific heat c_p/T versus T plot in the temperature range between 1.8 and 11 K in various magnetic fields is shown in Fig. 5. A sharp anomaly with the transition temperature $T_c = 9.7$ K is observed in zero magnetic field, confirming bulk superconductivity of $\text{Mo}_8\text{Ga}_{41}$. The temperature of the transition was determined by a graphical equal-areas approximation (entropy conserving) for each field H . Magnetic field shifts the transition to lower temperatures, and finally, no sign of the transition is observed in the $H = 10$ T magnetic field at temperatures above 1.8 K. Using the data obtained in different magnetic fields, we calculated the upper critical field $\mu_0 H_{c2}(T)$ of $\text{Mo}_8\text{Ga}_{41}$ (Fig. 8).

A closer view at the specific-heat anomaly in zero magnetic field is presented in Fig. 6. We used line approximation of the data just below and above the transition to extract the value of the jump in the specific heat at T_c . The corresponding construction is shown by blue lines in Fig. 6, with the vertical blue line located at the transition temperature $T_c = 9.7$ K.

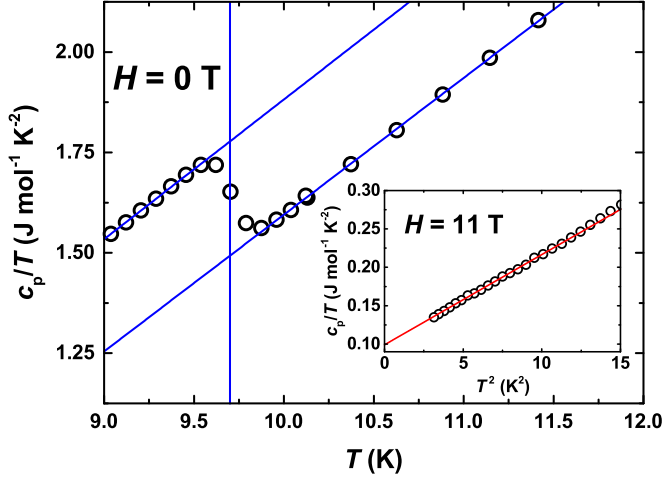


FIG. 6. The specific-heat anomaly in zero magnetic field. The solid curve is a construction to estimate the specific-heat jump at $T = T_c$. The inset shows c_p/T vs T^2 plot in $H = 11$ T magnetic field, the solid curve represents the linear fit of the data.

According to this approximation, we obtained $\Delta c_p/T_c = 280 \text{ mJ mol}^{-1} \text{ K}^{-2}$, although the $\Delta c_p/T_c$ value might be a bit overestimated by this method due to the smoothness of the superconducting transition.

The normal-state specific heat of $\text{Mo}_8\text{Ga}_{41}$, measured in the 11-T magnetic field, is shown in the inset of Fig. 6. The c_p/T versus T^2 plot can be fitted by the equation $c_p/T = \gamma_N + \beta T^2$ at temperatures between 1.77 and 3.53 K, giving $\gamma_N = 99.1(5) \text{ mJ mol}^{-1} \text{ K}^{-2}$ and $\beta = 11.76(7) \text{ mJ mol}^{-1} \text{ K}^{-4}$, which yields the Debye temperature of $\Theta_D = 201$ K. Thus, the normalized jump of the specific heat at T_c is $\Delta c_p/\gamma_N T_c = 2.83$. This value indicates a much stronger electron-phonon coupling in the superconducting state of $\text{Mo}_8\text{Ga}_{41}$ than the weak-coupling BCS limit, where $\Delta c_p/\gamma_N T_c = 1.43$ is expected. The electron-phonon coupling constant λ_{ep} can be estimated using the equation

$$\lambda_{ep} = \frac{\gamma_N}{\gamma_{\text{bare}}} - 1, \quad (1)$$

where γ_N and $\gamma_{\text{bare}} = \frac{\pi^2 k_B^2}{3} N(E_F)$ are the experimental and calculated values of the Sommerfeld coefficient of the electronic specific heat, respectively, and $N(E_F)$ is the density of states at the Fermi level. From the band-structure calculations we obtained $N(E_F) = 22.36 \text{ st. eV}^{-1} \text{ f.u.}^{-1}$, yielding $\gamma_{\text{bare}} = 52.7 \text{ mJ mol}^{-1} \text{ K}^{-2}$ and $\lambda_{ep} = 0.88$. In addition, λ_{ep} can be estimated in the single-gap superconductivity approximation using McMillan's formula [26]:

$$\lambda_{ep} = \frac{1.04 + \mu^* \ln\left(\frac{\Theta_D}{1.45 T_c}\right)}{(1 - 0.62 \mu^*) \ln\left(\frac{\Theta_D}{1.45 T_c}\right) - 1.04}, \quad (2)$$

where μ^* is the Coulomb pseudopotential, Θ_D is the Debye temperature, and T_c is the superconducting transition temperature. The Coulomb pseudopotential μ^* is equal to 0.1 in the case of nearly free-electron metals, as confirmed empirically for Zn. For many other transition metals, the empirical values of μ^* vary only slightly around 0.13, therefore, $\mu^* = 0.1$ and 0.15 values could be used for estimating the plausible

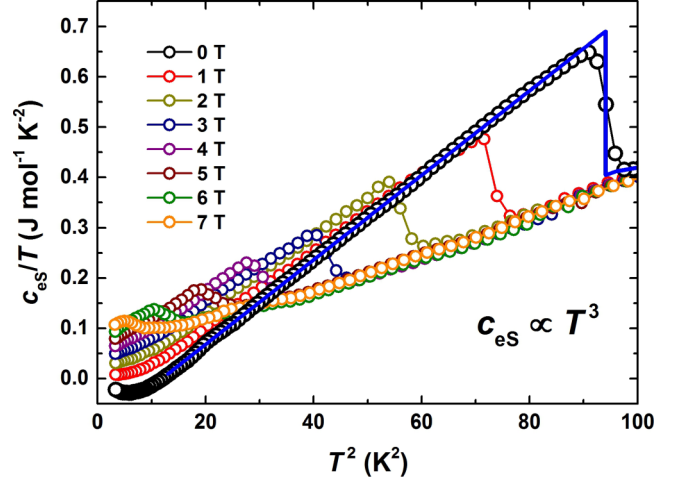


FIG. 7. Electronic specific-heat c_{es}/T vs T^2 plot in various magnetic fields together with $\propto T^3$ behavior for $H = 0$ T, which is shown by the solid blue line.

range of λ_{ep} [26]. The values of $\Theta_D = 201$ K and $T_c = 9.7$ K, obtained above from the heat-capacity data, yield $\lambda_{ep} = 0.90$ and 1.06 for $\mu^* = 0.1$ and 0.15, respectively. Thus, we find a good agreement between the λ_{ep} values, calculated using Eqs. (1) and (2). Henceforth, we will take $\lambda_{ep} = 0.9$, which corresponds to $\mu^* = 0.1$ and $\gamma_{\text{bare}} = 52.7 \text{ mJ mol}^{-1} \text{ K}^{-2}$.

The obtained high value of λ_{ep} implies strong electron-phonon coupling in the superconducting state of $\text{Mo}_8\text{Ga}_{41}$. Together with the unusually high value of $\Delta c_p/\gamma_N T_c = 2.83$, it indicates that the superconductivity of $\text{Mo}_8\text{Ga}_{41}$ significantly deviates from the BCS limit. To analyze the superconducting state in more detail, we calculated the electronic contribution to the heat capacity by subtracting the βT^3 lattice term from the $c_p(T)$ data. The resulting c_{es}/T versus T^2 plot in various magnetic fields is shown in Fig. 7. Unfortunately, the subtraction resulted in negative values of c_{es} in zero magnetic field below 3.5 K, which is, without doubt, due to the loss of accuracy in the estimation of β . However, negative values of c_{es} are not observed in higher magnetic fields. Moreover, we found that $c_{es}(T) \propto T^3$ in the superconducting state at temperatures above 3 K (for $H = 0$ T the corresponding construction is shown by blue line in Fig. 7). This additionally evidences non-BCS-type superconductivity of $\text{Mo}_8\text{Ga}_{41}$. At low temperatures, the heat-capacity data exhibit an anomaly, which is seen as the upturn of c_{es} in zero magnetic field. This anomaly may be attributed either to a small fraction of impurities in the specimen or to a nontrivial gap structure of the superconducting state. Due to the low-temperature anomaly, it remains unclear whether or not c_{es} of $\text{Mo}_8\text{Ga}_{41}$ is compatible with a nodal structure.

E. Lower and upper critical magnetic fields

From the magnetic field dependencies of magnetization, electrical resistivity, and heat capacity, we obtained the upper critical field of $\text{Mo}_8\text{Ga}_{41}$, which is shown in Fig. 8. The $\mu_0 H_{c2}(T)$ data from $M(H)$ and c_p perfectly coincide. The deviation of the upper critical field values, obtained from

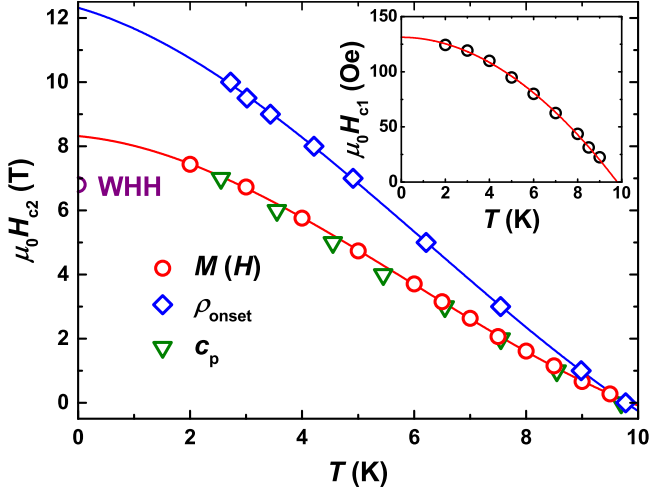


FIG. 8. Upper critical field $\mu_0 H_{c2}(T)$ of $\text{Mo}_8\text{Ga}_{41}$, determined from the magnetization, heat-capacity, and electrical resistivity measurements. The solid lines represent an extrapolation of the data by the second-order polynomial. Lower critical field $\mu_0 H_{c1}(T)$ is shown in the inset. The solid red line is a fit of the data, as described in the text.

the resistivity measurements, is likely due to the influence of surface superconductivity, which results in $\mu_0 H_{c3}(T)$. Regarding details of the resistivity measurements, we expect surface superconductivity emerging in each cross-sectional area of the sample, thus influencing the upper critical field substantially. From a free extrapolation by the second-order polynomial, we obtained $\mu_0 H_{c3}(0) = 12.3$ T from ρ_{onset} and $\mu_0 H_{c2}(0) = 8.3$ T from $M(H)$, yielding $\mu_0 H_{c3}(0)/\mu_0 H_{c2}(0) = 1.5$. In the ideal case $\mu_0 H_{c3}(0)/\mu_0 H_{c2}(0) = 1.7$ [27], however, deviations are known for a number of type-II superconducting alloys, for which the values of $\mu_0 H_{c3}(0)/\mu_0 H_{c2}(0)$ between 1.4 and 2.1 are found experimentally [27,28].

We will further discuss $\mu_0 H_{c2}(T)$ from $M(H)$ and c_p , only. All the curves vary linearly with T down to $0.4T_c$, thus, the upper critical field $\mu_0 H_{c2}(0)$ can be estimated using the Werthamer-Helfand-Hohenberg (WHH) formula for the clean limit: $\mu_0 H_{c2}(0) = -0.693T_c(\frac{d\mu_0 H_{c2}(T)}{dT})|_{T_c}$ [29]. Using the values of $\frac{d\mu_0 H_{c2}(T)}{dT}|_{T_c} = -1$ T/K and $T_c = 9.8$ K, we obtained $\mu_0 H_{c2}(0) = 6.8$ T. Alternatively, a free extrapolation by the second-order polynomial, which is shown by the red line in Fig. 8, leads to the estimated value of the upper critical field $\mu_0 H_{c2}(0) = 8.3$ T from the $M(H)$ data. The observed value shows a clear enhancement with respect to the Werthamer-Helfand-Hohenberg prediction, consistent with the strong electron-phonon coupling inferred from the the jump in the specific heat. The $\mu_0 H_{c2}(0)$ value corresponds to the Ginzburg-Landau coherence length of $\xi_{\text{GL}} = 158$ Å, as calculated from $\mu_0 H_{c2}(0) = \frac{\Phi_0}{2\pi\xi_{\text{GL}}^2}$, where Φ_0 is the flux quantum $h/2e$. $\mu_0 H_{c2}(0)$ is significantly lower than the Pauli-paramagnetic limit for weak electron-phonon coupling, which is $\mu_0 H_P = 1.86T_c = 18.2$ T. The obtained value of $\mu_0 H_P$ yields the Maki parameter $\alpha = \sqrt{2}\mu_0 H_{c2}(0)/\mu_0 H_P = 0.53$, where $\mu_0 H_{c2}(0)$ is the WHH limit of the upper critical field. Alternatively, the Maki parameter α can be derived from γ_N and ρ_0 using the formula applicable in the dirty

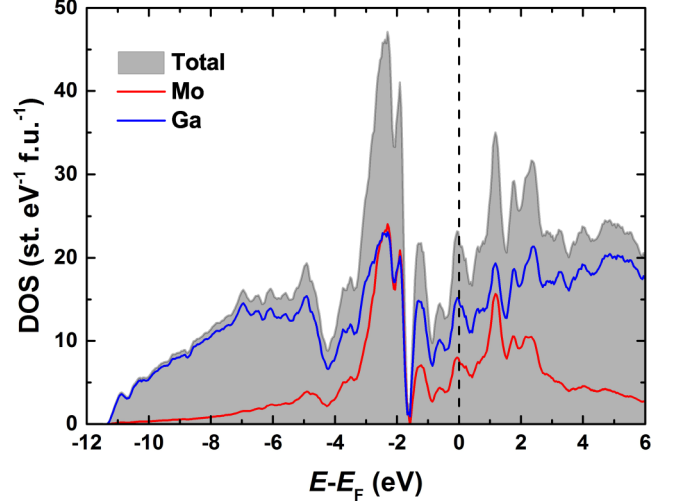


FIG. 9. Calculated electronic density of states (DOS) for $\text{Mo}_8\text{Ga}_{41}$. The Fermi level is indicated by the dashed line.

limit [29]:

$$\alpha = \frac{3e^2\hbar\gamma_N\rho_0}{2m_e\pi^2k_B^2V_m}, \quad (3)$$

where γ_N is the experimental value of the Sommerfield coefficient, ρ_0 is the normal-state resistivity extrapolated to zero temperature, and V_m is the molar volume. Using the values of $\gamma_N = 99.1(5)$ mJ mol⁻¹ K⁻² and $\rho_0 = 0.221(5)$ mΩ cm, we obtained $\alpha = 1.02$. The difference between the two estimates of α may arise from uncertainties in determining the absolute value of resistivity ρ_0 on a polycrystalline sample. Nevertheless, both estimates of α indicate that the SC transition should be a second-order phase transition, as expected for a type-II superconductor.

The inset of Fig. 8 shows the lower critical field $\mu_0 H_{c1}(T)$ of $\text{Mo}_8\text{Ga}_{41}$ obtained from the magnetization data. The $\mu_0 H_{c1}(T)$ data can be satisfactorily fitted using the equation $\mu_0 H_{c1}(T) = \mu_0 H_{c1}(0)[1 - (\frac{T}{T_c})^\beta]$. The fitting curve is presented as a red line in the inset of Fig. 8. Assuming that the transition temperature is $T_c = 9.8$ K, we obtained $\mu_0 H_{c1}(0) = 131(2)$ Oe and $\beta = 1.95(5)$. The lower critical field $\mu_0 H_{c1}(0)$, which indicates the appearance of flux lines in the sample volume, is much lower than the upper critical field $\mu_0 H_{c2}(0)$ of $\text{Mo}_8\text{Ga}_{41}$, as it is usually observed in type-II superconductors.

F. Electronic structure

The calculated electronic density of states (DOS) for $\text{Mo}_8\text{Ga}_{41}$ is shown in Fig. 9. In general, the energy spectrum of $\text{Mo}_8\text{Ga}_{41}$ is similar to those calculated for the isostructural compounds V_8Ga_{41} and $\text{T}_8\text{Ga}_{41-y}\text{Zn}_y$ [30] ($T = \text{V, Cr, Mn}$). The energetically low-lying region between -11 and -4 eV is primarily composed by Ga 4s and 4p contributions with a small admixture of Mo 4d states. At higher energies above -4 eV, the strong bonding between Ga and Mo species is observed. The mixing of Ga 4p and Mo 4d orbitals results in the sharp peak of the DOS reaching almost 50 st. eV⁻¹ f.u.⁻¹ at the relative energy of -2.3 eV. This peak is separated from the rest of the spectrum by the dip, located at -1.6 eV. The DOS near

the Fermi level at energies between -1.6 eV and 3 eV also has a sharp peak structure with the Fermi level located close to the local maximum of the DOS, composed mainly of Ga $4p$ and Mo $4d$ contributions. The resulting high value of the DOS at the Fermi level is $N(E_F) = 22.36$ st. $\text{eV}^{-1} \text{f.u.}^{-1}$ yields the bare Sommerfield coefficient of the electronic specific heat $\gamma_{\text{bare}} = 52.7$ $\text{mJ mol}^{-1} \text{K}^{-2}$.

In the $\text{Mo}_{8-x}\text{V}_x\text{Ga}_{41}$ solid solution, the substitution of V for Mo results in the reduced number of valence electrons per formula unit. Consequently, the Fermi level shifts to lower energies resulting in the density of states at the Fermi level $N(E_F) = 25.96$ st. $\text{eV}^{-1} \text{f.u.}^{-1}$ and 23.25 st. $\text{eV}^{-1} \text{f.u.}^{-1}$ for $x = 1$ and 1.9 , respectively. These values only slightly exceed the $N(E_F)$ value obtained for the unsubstituted $\text{Mo}_8\text{Ga}_{41}$. As a result, the DOS at the Fermi level remains high, thus remaining favorable for the superconductivity. Moreover, a moderate increase of T_c is expected from the derived values of $N(E_F)$.

G. $\text{Mo}_{8-x}\text{V}_x\text{Ga}_{41}$ solid solution

The fact that $\text{Mo}_8\text{Ga}_{41}$ and V_8Ga_{41} intermetallic compounds possess the same type of crystal structure motivated us to investigate the formation of the $\text{Mo}_{8-x}\text{V}_x\text{Ga}_{41}$ solid solution. Crystals of the solid solution were obtained by the high-temperature gallium flux technique using the Mo:V molar ratio of 7:1 and 6:2 in the reaction mixture for $x = 1$ and 2 , respectively. The obtained crystals were crushed and analyzed by the standard x-ray-diffraction technique, which showed that the specimen with $x = 1$ is single phase, and its diffraction pattern is consistent with the $\text{Mo}_8\text{Ga}_{41}$ structure type. Moreover, the $\text{Mo}_{7.0(2)}\text{V}_{1.0(1)}\text{Ga}_{41.0(2)}$ elemental composition was determined by EDX spectroscopy, and it perfectly agrees with the nominal one.

According to the XRD results, the specimen with $x = 2$ also represents the $\text{Mo}_8\text{Ga}_{41}$ -based solid solution, but additionally it contains a small admixture of the secondary V_8Ga_{41} -based phase. For this specimen, the averaged elemental composition of crystals was found to be $\text{Mo}_{6.1(1)}\text{V}_{1.9(2)}\text{Ga}_{41.0(1)}$ by energy-dispersive x-ray spectroscopy (EDXS). All these results suggest the formation of the limited solid solution $\text{Mo}_{8-x}\text{V}_x\text{Ga}_{41}$ with $x_{\text{max}} = 1.9(2)$.

Single-crystal XRD experiments were carried out to investigate the crystal structure of the solid solution at room temperature. Details of the crystal data collection and refinement are summarized in Table S1 in the Supplemental Material; the obtained atomic parameters and selected interatomic distances are given in Tables S2 and S3, respectively. According to the single-crystal XRD results, the solid solution crystallizes in the parent V_8Ga_{41} type of crystal structure. V atoms substitute Mo atoms almost evenly in two crystallographic positions, as it is seen from the refined occupation factors (s.o.f. in Table S2). Note that the total s.o.f. values were constrained to achieve the compositions determined by EDXS for each sample.

Thermodynamic and transport measurements suggest that the solid solution becomes superconducting at low temperatures, very similar to the parent $\text{Mo}_8\text{Ga}_{41}$ compound. The $\rho(T)$ curves measured in zero magnetic field for $x = 0, 1$, and 2 are given in Fig. 10. As in the case of $\text{Mo}_8\text{Ga}_{41}$, the solid solution exhibits metallic behavior with high absolute values of resistivity. The thermodynamic and transport measurements

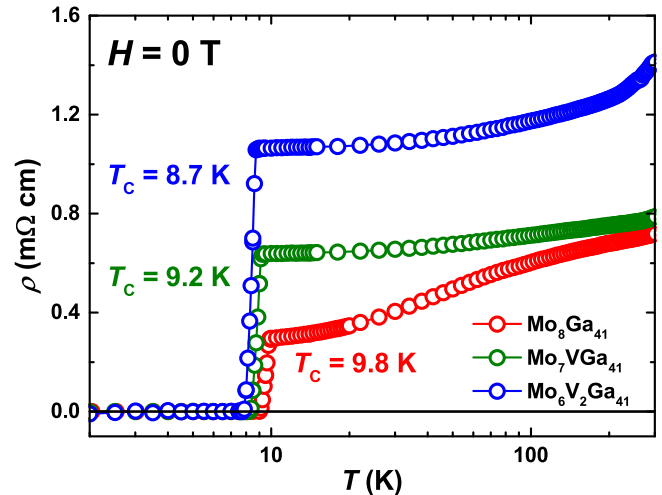


FIG. 10. Electrical resistivity of the $\text{Mo}_{8-x}\text{V}_x\text{Ga}_{41}$ solid solution for $x = 0, 1$, and 2 in zero magnetic field.

confirm the bulk superconductivity of the $\text{Mo}_{8-x}\text{V}_x\text{Ga}_{41}$ solid solution with $T_c = 9.8, 9.2$, and 8.7 K in zero magnetic field for $x = 0, 1$, and 2 , respectively. Thus, the sizable substitution of V for Mo atoms in the crystal structure has a rather weak effect on superconductivity, as expected from the high values of $N(E_F)$ for the solid solution. However, the reduction in T_c do not correlate with the evolution of $N(E_F)$, since the disorder induced by the random arrangement of Mo and V atoms in the crystal structure may also have an impact on T_c .

IV. CONCLUSIONS

Crystals of the intermetallic compound $\text{Mo}_8\text{Ga}_{41}$ and the limited solid solution on its base, $\text{Mo}_{8-x}\text{V}_x\text{Ga}_{41}$ with $x_{\text{max}} = 1.9(2)$, have been grown from the high-temperature Ga flux. Magnetization, specific heat, and transport measurements confirm bulk superconductivity of $\text{Mo}_8\text{Ga}_{41}$ with $T_c = 9.8$ K. Analysis of the specific-heat data gives evidence of various non-BCS-type features: (i) the normalized specific heat jump at T_c , $\Delta c_p / \gamma_N T_c = 2.83$, exceeds significantly the weak-coupling BCS limit, for which $\Delta c_p / \gamma_N T_c = 1.43$. From the specific-heat data we estimated the electron-phonon coupling constant $\lambda_{ep} = 0.9$, that is consistent with the strong-coupling regime. (ii) The electronic contribution to the specific heat c_{es}/T below T_c significantly deviates from the conventional BCS-type behavior, and a power law with $c_{es}(T) \propto T^3$ is observed above 3 K instead. All these facts evidence the strong-coupling non-BCS-type behavior of $\text{Mo}_8\text{Ga}_{41}$ and the persistence of this regime upon vanadium doping. Future studies of this material are desirable.

ACKNOWLEDGMENTS

The authors acknowledge insightful discussions with E. Joon and W. Schnelle, and thank V. Tafeenko for the help with single-crystal XRD experiments. The work has been supported by the Russian Foundation for Basic Research, Grant No. 14-03-31181-mol_a, and by the Mobilitas program of the ESF, Grant No. MTT77. A.A.T. is also grateful for the financial support by the Federal Ministry for Education and Research

under the Sofja Kovalevskaya Award of the Alexander von Humboldt Foundation. We acknowledge the use of a STOE

STADIVARI single-crystal x-ray diffractometer purchased under the Lomonosov MSU program of development.

-
- [1] C. P. Poole, *Handbook of Superconductivity* (Academic, London, 2000).
 - [2] N. Morton, B. W. James, G. H. Wostenholm, D. G. Pomfret, M. R. Davies, and J. L. Dykins, *J. Less-Common Met.* **25**, 97 (1971).
 - [3] E. Bauer, G. Rogl, X. Q. Chen, R. T. Khan, H. Michor, G. Hilscher, E. Royanian, K. Kumagai, D. Z. Li, Y. Y. Li, R. Podloucky, and P. Rogl, *Phys. Rev. B* **82**, 064511 (2010).
 - [4] A. B. Karki, Y. M. Xiong, I. Vekhter, D. Browne, P. W. Adams, D. P. Young, K. R. Thomas, J. Y. Chan, H. Kim, and R. Prozorov, *Phys. Rev. B* **82**, 064512 (2010).
 - [5] I. Bonalde, H. Kim, R. Prozorov, C. Rojas, P. Rogl, and E. Bauer, *Phys. Rev. B* **84**, 134506 (2011).
 - [6] E. Bauer, C. Sekine, U. Sai, P. Rogl, P. K. Biswas, and A. Amato, *Phys. Rev. B* **90**, 054522 (2014).
 - [7] C. Candolfi, B. Lenoir, A. Dauscher, C. Bellouard, J. Hejtmánek, E. Šantavá, and J. Tobola, *Phys. Rev. Lett.* **99**, 037006 (2007).
 - [8] V. H. Tran, W. Miiller, and Z. Bukowski, *Phys. Rev. Lett.* **100**, 137004 (2008).
 - [9] R. Khasanov, P. W. Klamut, A. Shengelaya, Z. Bukowski, I. M. Savić, C. Baines, and H. Keller, *Phys. Rev. B* **78**, 014502 (2008).
 - [10] R. Khasanov, A. Shengelaya, I. M. Savić, C. Baines, and H. Keller, *Phys. Rev. B* **82**, 016501 (2010).
 - [11] V. H. Tran, A. D. Hillier, D. T. Adroja, and Z. Bukowski, *Phys. Rev. B* **78**, 172505 (2008).
 - [12] V. H. Tran, A. D. Hillier, and D. T. Adroja, *Phys. Rev. B* **82**, 016502 (2010).
 - [13] W. N. Dong, J. Pan, J. Zhang, X. C. Hong, L. P. He, S. Y. Zhou, J. K. Dong, and S. Y. Li, *Solid State Commun.* **195**, 84 (2014).
 - [14] A. Bezing and K. Yvon, *J. Less-Common Met.* **99**, L27 (1984).
 - [15] K. Yvon, *Acta Crystallogr., Sect. B: Struct. Crystallogr. Cryst. Chem.* **31**, 117 (1975).
 - [16] V. Petříček, M. Dušek, and L. Palatinus, *Z. Kristallogr.* **229**, 345 (2014).
 - [17] See Supplemental Material at <http://link.aps.org/supplemental/10.1103/PhysRevB.93.064501> for details of the single-crystal XRD experiments and crystal structure refinement.
 - [18] M. C. Burla, M. Camalli, B. Carrozzini, G. L. Cascarano, C. Giacovazzo, G. Polidori, and R. Spagna, *J. Appl. Crystallogr.* **36**, 1103 (2003).
 - [19] L. M. Gelato and E. Parthé, *J. Appl. Crystallogr.* **20**, 139 (1987).
 - [20] J. P. Perdew and Y. Wang, *Phys. Rev. B* **45**, 13244 (1992).
 - [21] K. Koepernik and H. Eschrig, *Phys. Rev. B* **59**, 1743 (1999).
 - [22] P. E. Blöchl, O. Jepsen, and O. K. Andersen, *Phys. Rev. B* **49**, 16223 (1994).
 - [23] O. Gunnarsson, M. Calandra, and J. E. Han, *Rev. Mod. Phys.* **75**, 1085 (2003).
 - [24] Z. Fisk and G. W. Webb, *Phys. Rev. Lett.* **36**, 1084 (1976).
 - [25] G. A. Bain and J. F. Berry, *J. Chem. Educ.* **85**, 532 (2008).
 - [26] W. L. McMillan, *Phys. Rev.* **167**, 331 (1968).
 - [27] D. Saint-James, G. Sarma, and E. J. Thomas, *Type II Superconductivity* (Elsevier Science & Technology, New York, 1969).
 - [28] C. F. Hempstead and Y. B. Kim, *Phys. Rev. Lett.* **12**, 145 (1964).
 - [29] N. R. Werthamer, E. Helfand, and P. C. Hohenberg, *Phys. Rev.* **147**, 295 (1966).
 - [30] P. Viklund, C. Svensson, S. Hull, S. I. Simak, P. Berastegui, and U. Häussermann, *Chem. Eur. J.* **7**, 5143 (2001).